Available online at www.sciencedirect.com

ScienceDirect

Acta Materialia 57 (2009) 2919–2932

Acta MATERIALIA

www.elsevier.com/locate/actamat

Designing highly toughened hybrid composites through nature-inspired hierarchical complexity

M.E. Launey [a], E. Munch [a], D.H. Alsem [a,b], H.B. Barth [c,d], E. Saiz [a], A.P. Tomsia [a], R.O. Ritchie [a,d,*]

[a] *Materials Sciences Division, Lawrence Berkeley National Laboratory, Berkeley, CA 94720, USA*
[b] *National Center for Electron Microscopy, Lawrence Berkeley National Laboratory, CA 94720, USA*
[c] *Experimental Systems Group, Lawrence Berkeley National Laboratory, Berkeley, CA 94720, USA*
[d] *Department of Materials Science & Engineering, University of California, Berkeley, CA 94720, USA*

Received 12 February 2009; received in revised form 28 February 2009; accepted 1 March 2009
Available online 6 April 2009

Abstract

The notion of replicating the unique fracture resistance of natural composites in synthetic materials has generated much interest but has yielded few real technological advances. Here we demonstrate how using ice-templated structures, the concept of hierarchical design can be applied to conventional compounds such as alumina and poly(methyl methacrylate) (PMMA) to make bulk hybrid materials that display exceptional toughness that can be nearly 300 times higher (in energy terms) than either of their constituents. These toughnesses far surpass what can be expected from a simple "rule of mixtures"; for a ~80% Al_2O_3–PMMA material, we achieve a K_{Jc} fracture toughness above 30 MPa m$^{1/2}$ at a tensile strength of ~200 MPa. Indeed, in terms of specific strength and toughness, these properties for alumina-based ceramics are at best comparable to those of metallic aluminum alloys. The approach is flexible and can be readily translated to multiple material combinations.
Published by Elsevier Ltd. on behalf of Acta Materialia Inc.

Keywords: Ceramics; Composites; Toughness; Casting

1. Introduction

As existing structural materials reach their performance limits, one of the major scientific challenges for the 21st century is the development of new stronger and tougher lightweight structural materials to support advances in diverse strategic fields from building to transportation or energy. This is a challenge that can only be met through an understanding of the relationships between materials architecture and mechanical response, spanning not simply microstructure but encompassing the influence of structural parameters acting at multiple length scales, from the atomic to the macro levels, and their interactions. Furthermore, it will be essential to develop new fabrication techniques that are able to synthesize such materials in bulk form.

One approach in this quest for the design of new and superior structural materials is by mimicking the architecture of natural/biological materials and structures [1,2]. Nature combines readily available compounds that typically exhibit poor macroscale mechanical properties, e.g. brittle biological ceramics and compliant macromolecules, to produce composites, such as bone, nacre or tooth dentin, that are far stronger and tougher than could be expected from the simple mixture of their individual components [3,4]. The prospect of extending natural designs to multiple material combinations is very appealing, but an understanding of how natural structures achieve their unique mechanical response has only recently begun to

---

[*] Corresponding author. Address: Department of Materials Science & Engineering, University of California, Berkeley, CA 94720, USA. Tel.: +1 510 486 5798; fax: +1 510 643 5792.
E-mail address: RORitchie@lbl.gov (R.O. Ritchie).

1359-6454/$36.00 Published by Elsevier Ltd. on behalf of Acta Materialia Inc.
doi:10.1016/j.actamat.2009.03.003

emerge. It is clear that natural materials [4–7] generate their fracture resistance or toughness primarily by extrinsic mechanisms [8] which "shield" an advancing crack from the applied load. These mechanisms, which are quite different to those that toughen metals, for example, are simultaneously created at multiple dimensions, literally from nano- to macro-scales. From a fracture mechanics perspective, they generate a characteristic crack resistance curve (*R*-curve) behavior where the fracture resistance actually increases with crack extension; in other words, these materials develop the majority of their toughening during crack growth and not during crack initiation [9].

A major difference between natural and synthetic materials is clearly in the way that they are made. Nature grows complex structures from the "bottom up" using the principles of biologically controlled self-assembly [3,4]. However, this approach is generally not feasible for making synthetic materials in practical sizes with severe time constraints. Although there are several outstanding examples of materials fabricated in the laboratory by applying physicochemical principles taken from the growth of natural composites, these are invariably limited to thin films or microscopic samples [10–14]. Largely because of this, the field of biomimicry has generated few practical new materials. The key challenge here is to find "top-down" fabrication approaches that are able to mimic natural structural designs over as many length scales as possible.

In this work, freeze casting (also known as ice-templating) is used to fabricate bulk hybrid materials with unique hierarchical structures modeled on the structure of nacre (abalone shell). This technique uses the freezing of ceramic suspensions to form porous or dense ceramics with complex shapes and architectures. In particular, when freezing of the suspensions is carried out directionally using a temperature gradient, it is possible to fabricate lamellar scaffolds whose microstructure resembles that of the inorganic component of nacre at multiple length scales [15–17]. Here we show how this technology can be used to build nacre-like composites by filling the lamellar alumina scaffolds with a second, relatively soft, organic phase (poly(methyl methacrylate), PMMA), which acts as the non-load-bearing "lubricant" phase. The combination of alumina and PMMA allows the fast, systematic exploration of the effect of structural parameters at multiple length scales in the mechanical response. The final materials can have ceramic contents up to ~80 vol.% and, like their natural counterparts, exhibit rising *R*-curve behavior with fracture toughnesses up to 300 times higher (in energy terms) than their main constituent, Al_2O_3. In this regard, they represent the toughest ceramic-based materials ever made. Such unprecedented mechanical behavior is interpreted in terms of the prevalent mechanisms of microstructural damage and toughening, incorporating the concept of the "lubricant phase". Our intent is to incorporate the design lessons and fabrication technologies from this work in the development of novel hybrid materials that will combine diverse phases (e.g. metal–ceramic) to exhibit further unique combinations of strength and toughness.

2. Materials and methods

2.1. Processing

Lamellar alumina scaffolds were prepared by freeze-casting water-based suspensions. The suspensions (solid content 50 wt.%) were prepared by dispersing submicrometer alumina powders (SM8 high-purity submicrometer alumina powder, Baikowski) in deionized water with alumina balls. An ammonium polymethacrylate anionic dispersant (Darvan CN, R.T. Vanderbilt Co., Norwalk, CT, 1.4 wt.% of the powder) and an organic binder (polyvinylalcohol, 1.4 wt.% of the powder) were added to achieve a good powder dispersion and ensure the integrity of the ceramic structure after eliminating the water. Sucrose (β-D-fructofuranosyl α-D-glucopyranoside, 4 wt.% of the water content) was also added to provide a binder and to control the structure of the growing ice crystals, and to ensure the formation of fine ceramic lamellae with a characteristic microscopic roughness [18]. The suspensions were placed in cylindrical Teflon molds (25–50 mm diameter, 25–50 mm tall) sitting on a copper cold finger. The temperature of this cold finger was monitored and manipulated by combining a cold bath with ring heaters (Fig. 1). In order to obtain parallel ceramic lamellae aligned over macroscopic dimensions (centimeters), the copper surface where the ice nucleates was scratched unidirectionally with silicon carbide paper (grade P400) and vibration was applied to the mold during freezing [18]. The cold finger was cooled to −80 °C with the cooling rate varying between 1 and 20 °C min^{-1}. The frozen samples were then freeze-dried to sublimate the water and subsequently fired in air at 400 °C for 2 h to remove the organics and afterwards sintered at 1500 °C for 2 h to densify the ceramic lamellae. This resulted in a bulk scaffold, several centimeters in size (Fig. 2), formed by macroscopically oriented dense lamellae.

The ceramic scaffolds with finer lamellae (~5 μm wide, produced with a cold finger cooling rate of 20 °C min^{-1}) were used as the base for the fabrication of ceramic "brick-and-mortar" structures with ~20 vol.% porosity. The scaffolds were infiltrated with a short-chain polymer with a low melting point (paraffin wax) that acted as a sacrificial phase. The infiltrated scaffolds were uniaxially pressed at 80 °C, just above the melting point of the organic phase, at ~50–100 MPa. While liquid, the polymer flows and allows the densification of the ceramic structure, and after cooling it holds the bricks together for transfer into an air furnace. A thermal treatment in air was applied to remove the organic phase from the structure (2 h at 400 °C) and to promote densification (2 h at 1500 °C). Finally the samples were pressed isostatically at 1.4 GPa followed by a new sintering step (2 h at 1500 °C) to promote the formation of inorganic (ceramic) bridges between the bricks.

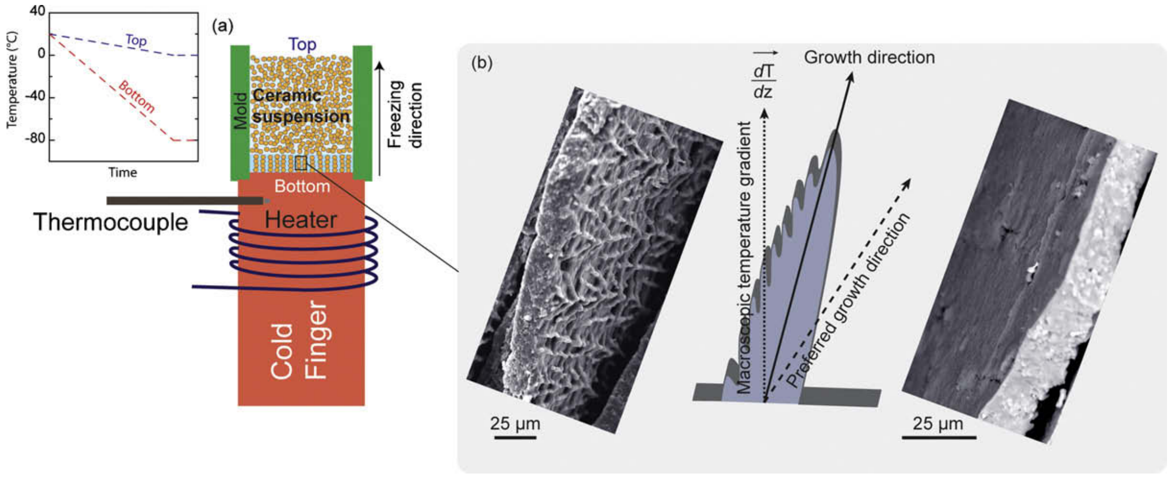

Fig. 1. (a) The freeze-casting set-up showing how the ceramic suspension is placed on top of a cold finger that is cooled at a constant rate (bottom line in the graph) in order to form a temperature gradient that promotes the formation of lamellar ice. The ice expels the ceramic particles as it grows to leave a layered ceramic structure after water removal. (b) The balance between imposed (parallel to the temperature gradient) and crystallographic preferred growth directions results in a characteristic dendritic roughness in one of the sides of the growing ice crystals. This roughness is replicated in the surface of the ceramic lamellae.

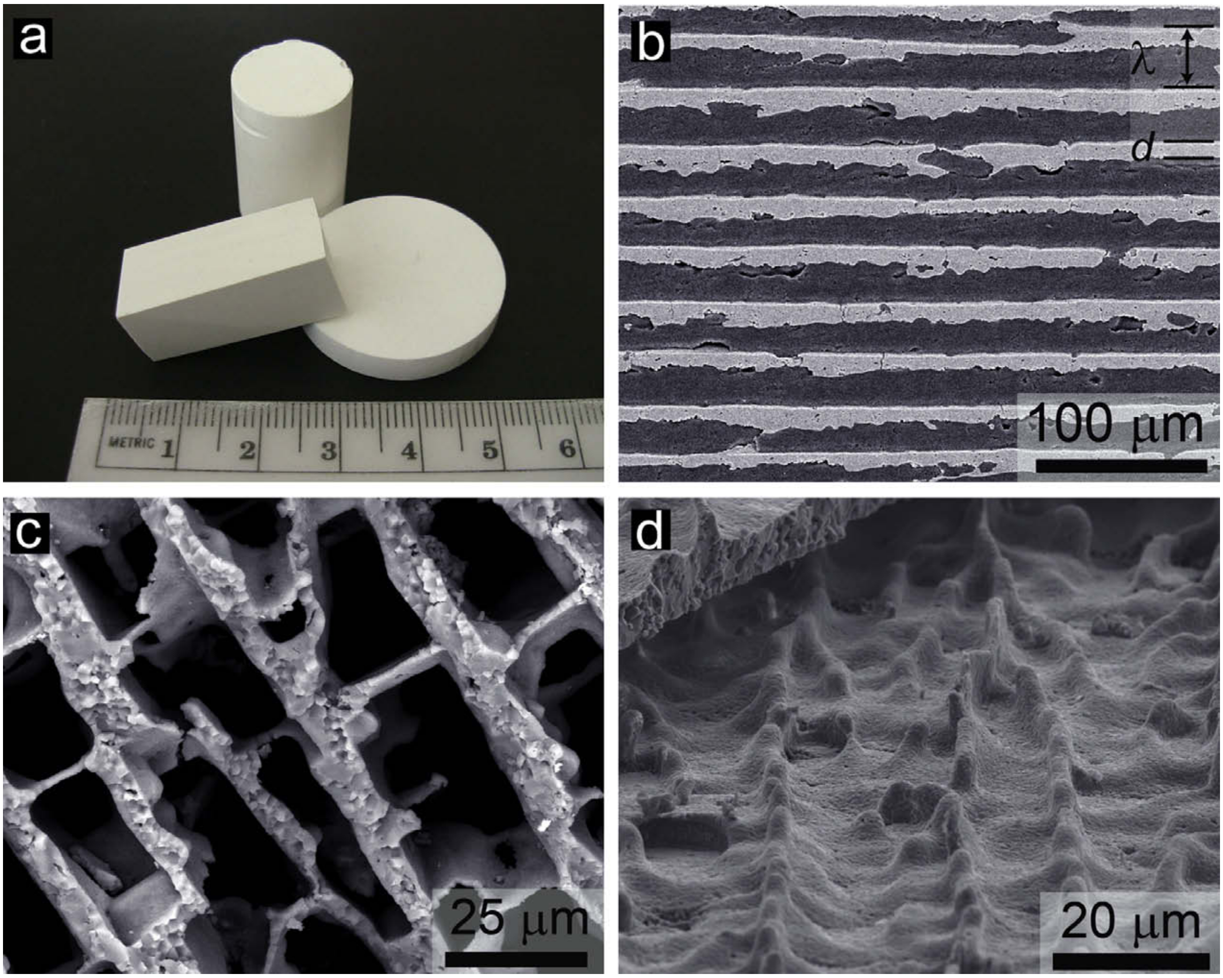

Fig. 2. (a) Porous scaffolds of practical dimensions obtained by freeze-casting of ceramic suspensions. The control of the processing conditions leads to macroscopic samples that exhibit (b) lamellar structures oriented over several centimeters followed by polymer infiltration (the lighter phase is the ceramic; the dark phase is the polymer). λ represents the microstructural wavelength, and d the thickness of the lamellae. (c) The process results in the formation of ceramic bridges between lamellae due to the trapping of ceramic particles by the growing ice. (d) By using sucrose as an additive to the freeze-casting slurry the growing ice crystals develop a characteristic surface topography that translates into a microscopic roughness in the ceramic walls.

The scaffolds were infiltrated with a second polymeric phase by a free radical polymerization in bulk of methylmethacrylate (MMA) initiated by 2,2′-azobisisobutyronitrile (AIBN, 0.5 wt.% in MMA) at 70 °C for 12 h. The infiltrated samples were annealed in an oven at 150 °C for 2 h in gaseous nitrogen to complete the polymerization reaction and slowly cooled (~1 °C min^{-1}) to room temperature to minimize thermally induced residual stresses.

In order to enhance adhesion at the organic/inorganic interface, 3-(trimethoxysilyl)propyl methacrylate (γ-MPS) was grafted on the surface of selected scaffolds prior to the polymer infiltration [19]. The scaffolds were first immersed in a Piranha solution (1:1 H_2O_2:30 vol.% H_2SO_4) for 10–15 min in order to promote the formation of hydroxyl groups in the internal surfaces [20]. After carefully rinsing with deionized water, the scaffold was immersed in a solution of the grafting agent (γ-MPS), in acetone (50 vol.% acetone, 50 vol.% γ-MPS) for 6–12 h. The objective was to form a covalent bond between the γ-MPS molecules and the hydroxyl groups on the ceramic surface. The γ-MPS acts as a coupling agent between the PMMA and the alumina, yielding stronger adhesion at the organic/inorganic interface after infiltration.

The infiltration of the grafted scaffolds was performed using two polymerization steps. The first step was a free radical polymerization of MMA initiated by AIBN run in a solvent (toluene, 2:1 toluene:MMA by weight) with a relatively high initiator concentration (1 wt.% AIBN in MMA, 1 h at 70 °C in N_2). The solvent helps to minimize the self-acceleration phenomenon inherent in the free radical polymerization reaction and allows an increase in the amount of activator. The high concentration of activator maximizes the chances for radicals to develop on γ-MPS molecules bonded to the ceramic surface, leading to chemically grafted PMMA chains. After evaporation of the solvent, the infiltration was performed by the bulk free radical polymerization previously described for a non-grafted material.

The mechanical response of the hierarchical materials was compared to that of homogeneous particulate PMMA/Al_2O_3 nanocomposites, as well as dense PMMA and alumina. The nanocomposites were prepared by pressing uniaxially (20 MPa) the same Al_2O_3 powders used in the preparation of freeze-cast scaffolds to form pellets (diameter 30 mm, height 15 mm) which were then sintered in air at 1100 °C for 2 h. The resulting porous samples (20–45 vol.% porosity) were infiltrated with PMMA following the procedure described above for non-grafted materials. Dense alumina samples were obtained by slip casting a water-based ceramic suspension (60 wt.% of alumina powder in water). The suspensions for slip casting and freeze casting used the same starting powders and similar solid contents with identical sintering cycles. Slip casting was selected to prepare the reference ceramic materials because the ceramic forms through the packing of powders from a liquid suspension, as in freeze casting. Pure PMMA samples were obtained by the polymerization in bulk of methylmethacrylate initiated by AIBN (0.5 wt.% AIBN in MMA) for 8 h at 50 °C in nitrogen. The use of identical polymerization conditions led to polymers with identical molecular weights.

To compare the behavior of our hybrid composites with that of nacre, small beams were prepared from the nacreous layer of a red abalone shell (*Haliotus rufescens*). Raw samples were first cut from the shell using a low-speed diamond saw. The calcitic layer was ground away to leave the nacre and the samples were then lapped on both faces. Finally, thin samples were sliced to obtain the final beams (20 mm long, 2.3–2.4 mm wide and 1.2–1.4 mm thick). Samples were kept immersed in water so that they remained hydrated until testing.

Rectangular beams for bending tests with the tensile faces parallel to the ceramic layers were sectioned from the infiltrated scaffolds by using a water-cooled, low-speed diamond saw. The final specimens were 18–28 mm long, 1.3–1.5 mm thick (B) and 3.0–3.2 mm wide (W). Plane-strain fracture toughness, K_{IC}, and R-curve measurements were performed on single-edge notched bend (SE(B)) specimens. An initial notch was applied with a low-speed diamond saw and was subsequently sharpened by repeatedly sliding a razor blade over the saw-cut notch using a custom-made rig, while continually irrigating with 1 μm diamond slurry. The final micro-notches had a root radius of ~3–5 μm. Sharp cracks with initial crack lengths, a, of ~1.6–1.7 μm were generated in general accordance with ASTM standards [21]. The orientation of the notch was such that the nominal crack-growth direction was perpendicular to the ceramic layers.

Alumina SE(B) specimens (24 mm long, 6.0 mm wide and 2.4–2.5 mm thick) were fatigue pre-cracked using a half-chevron starter notch (in addition to a Vickers hardness indent placed at the notch tip) in order to facilitate crack initiation. SE(B) specimens of PMMA (22 mm long, 2.7–2.8 mm wide and 1.2–1.4 mm thick) and hydrated nacre were micro-notched. Prior to testing, all specimens were polished on both faces down to a 1 μm finish using diamond suspensions.

2.2. Mechanical characterization

2.2.1. Strength and K_{IC} measurements

Three-point bend tests were performed to generate quantitative stress–strain curves and measure the plane-strain fracture toughness, K_{IC}. The strength tests used a support span S of 12.5 mm and a displacement rate of 1 μm s^{-1} in general accordance with ASTM standards [22]. The toughness measurements were performed on SE(B) specimens, also using a support span of 12.5 mm. Values were determined by monotonically loading the specimens to failure at a constant displacement rate of 1 μm s^{-1}. All toughness tests satisfied the plane-strain and small-scale yielding requirements for valid K_{IC} measurement, as per ASTM standards [21]. All values presented represent at least an average of three measurements per configuration ($n \geqslant 3$).

2.2.2. *Fracture toughness J–R curve measurements*

Nonlinear-elastic fracture mechanics methods were used to evaluate the fracture toughness resistance in terms of the *J*-integral as a function of crack extension, Δa, under a monotonically increasing driving force. *R*-curves were measured on SE(B) specimens in situ in a scanning electron microscope using a three-point bending stage, again with $n \geqslant 3$. Tests were conducted in three-point bending with a span ($S = 12.5$ mm) to width ($W \sim 3.0$–3.2 mm) ratio of ~4, in accordance with ASTM standard E1820 [21]. The crosshead displacement was measured with a linear variable-displacement transducer, while the load was recorded using a 150 N load cell. Prior to in situ testing, specimens were coated with a ~20 nm thin layer of gold. *R*-curve determination was limited to small-scale bridging conditions, where the size of the zone of crack bridges behind the crack tip remained small compared to the in-plane test specimen dimensions. The use of nonlinear elastic fracture mechanics with the *J*-integral as the driving force for crack initiation and growth was employed to capture the contribution from inelastic deformation in the evaluation of the toughness of the hybrid composites.

The stress intensity at each measured crack length was calculated by measuring the nonlinear strain-energy release rate, *J*, where *J* is defined as the rate of change in potential energy under nonlinear-elastic conditions for a unit increase in crack area [21]. *J* was calculated from the applied load and instantaneous crack length according to ASTM standards [21], and was decomposed into its elastic and plastic contributions:

$$J = J_{\mathrm{el}} + J_{\mathrm{pl}}. \tag{1}$$

The elastic contribution J_{el} is based on linear-elastic fracture mechanics:

$$J_{\mathrm{el}} = \frac{K_{\mathrm{I}}^2}{E'}, \tag{2}$$

where K_{I} is the mode I stress-intensity factor, and $E' = E$ in plane stress and $E/(1 - \nu^2)$ in plane strain (ν is Poisson's ratio). For SE(B) specimens, K_{I} is given in terms of the applied load P by:

$$K_{\mathrm{I}} = \frac{PS}{BW^{3/2}} f(a/W), \tag{3}$$

where f is a non-dimensional function of the crack length a:

$$f(a/W) = \frac{3(a/W)^{1/2}[1.99 - (a/W)(1 - a/W)(2.15 - 3.93(a/W) + 2.7(a/W)^2)]}{2(1 + 2a/W)(1 - a/W)^{3/2}}. \tag{4}$$

Using the load-line displacements, the plastic component J_{pl} for a stationary crack in bending is given by:

$$J_{\mathrm{pl}} = \frac{1.9 A_{\mathrm{pl}}}{Bb}, \tag{5}$$

where A_{pl} is the plastic area under force vs. displacement curve, and b is the uncracked ligament length (W–a). To take in account the fact that the crack is advancing and that the ligament b is continuously decreasing, an incremental definition of Eq. (5) was used [21]:

$$J_{pl(i)} = \left[J_{\mathrm{pl}(i-1)} + \left(\frac{1.9}{b_{(i-1)}} \right) \left(\frac{A_{\mathrm{pl}(i)} - A_{\mathrm{pl}(i-1)}}{B} \right) \right] \left[1 - \frac{a_{(i)} - a_{(i-1)}}{b_{(i-1)}} \right]. \tag{6}$$

Provided all validity criteria [21] were met, *K*-based fracture toughness values were back-calculated from the *J* measurements using the standard *J*–*K* equivalence for nominally mode I fracture, specifically that $K_{\mathrm{J}} = (J.E')^{1/2}$.

2.3. *Microstructural characterization*

Microstructures were characterized using optical and electron microscopy. Image analysis and thermogravimetry were used to calculate the relative amounts of organic and inorganic phases. The density of the porous scaffolds was also measured by the Archimedes method. Total parameters micro X-ray computed tomography (μXCT) was employed to visualize in three dimensions the crack path and distribution of micro-damage after *R*-curve testing. The μXCT setup at the Lawrence Berkeley National Laboratory's Advanced Light Source is similar to standard tomography procedures [23]; samples are rotated in a monochromatic X-ray beam and the transmitted X-rays imaged via a scintillator, magnifying lens and a digital camera to give an effective voxel size in the reconstructed three-dimensional (3-D) image of 4.45 μm. The samples were scanned in absorption mode and the reconstructed images were obtained using a filtered back-projection algorithm. In absorption mode the grayscale values of the reconstructed image are representative of the absorption coefficient. To maximize the signal-to-noise ratio, the energy was selected at 15 keV; this optimizes the interaction between the X-rays and the sample. Two-dimensional images were taken every quarter of a degree between 0° and 180°. The data sets were reconstructed using the software Octopus [24] and the 3-D visualization was performed using Avizo™ software [25].

3. Results

3.1. *Microstructural features*

3.1.1. *Lamellar composites*

The controlled directional freezing of water-based ceramic suspensions was used to create porous ceramic scaffolds, several centimeters in size (Fig. 2a). By cooling the cold finger at a constant rate starting from room temperature it was possible to promote the directional growth of lamellar ice. The ice expels the ceramic particles as it grows; subsequent water sublimation and sintering results in a scaffold formed by ceramic layers of homogeneous thickness running continuously from the bottom to the top of the sample (Fig. 2c). The layers are dense and aligned over macroscopic dimensions (centimeters), and are connected by thin (⩽1 μm) ceramic bridges (Fig. 2c), with a grain size of the order of 1 μm.

A key characteristic of the freeze-casting process is the ability to manipulate the materials structure at multiple dimensions. The microstructural wavelength, λ, and the lamellae thickness, d (Fig. 2), are primarily a function of the ice-front velocity (controlled by the cooling rate of the cold finger) and to a lesser extent of the ceramic particle size [26,27]. The faster the speed of the freezing front (the faster the cooling rate of the finger), the finer the microstructural wavelength and the lamellae thickness. As our objective was to mimic the nacre structure and fabricate samples with the larger ceramic contents, we maximized the solid content of the suspensions. The maximum alumina concentrations that could be used to consistently fabricate lamellar materials with macroscopically oriented ceramic layers were of the order of 50 wt.% (∼20 vol.%). The porosity of the resulting scaffolds after sintering was ∼64 vol.% and the lamellae thickness, d, varied between ∼5 and 20 μm for cold finger cooling rates between 20 and 1 °C min^{-1}, respectively [26]. Faster ice growth can be achieved by reducing the temperature gradient during freezing (e.g. by using a top cold finger); however, this can result in a tilted lamellae growth as the ice growth direction depends on the balance between the preferred crystallographic orientation and that which is forced by the temperature gradients [26]. Eventually, the lamellae thickness is limited by the alumina particle size (∼1 μm after sintering). Subsequent infiltration with PMMA resulted in a composite with a uniform two-phase lamellar microstructure (Fig. 2b) with a ∼36 vol.% of ceramic phase as determined by both thermogravimetry and image analysis.

During the growth of ice, the balance between imposed (parallel to the temperature gradient) and crystallographic preferred growth directions result in a slight tilting of the ice lamellae and the formation of dendrites on one of the sides (Fig. 1). After removing the water, these dendrites are reflected in a characteristic roughness on one of the sides of the ceramic layers while the other remains very smooth at the microscopic level (Fig. 1). This roughness plays a critical role in controlling shear at the organic/inorganic interface during loading and can be manipulated using different additives in the suspension. The additives determine the shape of the growing ice crystals by modifying the interfacial tensions, the degree of supercooling ahead of the ice front and the viscosity and the phase diagram of the solvent (promoting, for example, the formation of fugitive phases that are eliminated during sintering) [18]. In the present study, the use of sucrose resulted in the formation of a characteristic microscopic roughness characterized by relatively smooth dendritic-like features, 1–5 μm high, running in the direction of solidification (Fig. 2d) on one of the lamellae sides [18,26].

3.1.2. Brick-and-mortar composites

Hot pressing of the lamellar material and subsequent sintering at 1500 °C resulted in brick-and-mortar architectures with large ceramic contents of up to 80 vol.% (Fig. 3a). The fine-grained (1 μm) alumina “bricks” were 5–10 μm wide and 20–100 μm long. After infiltrating these structures with PMMA, the polymer layers had an overall thickness of ∼1–2 μm; however, there were large regions in which the alumina bricks were separated by submicrometer polymer films (Fig. 3b). Another important feature of these brick-and-mortar architectures was the formation of a high density of ceramic bridges between bricks during sintering. These bridges (typically of submicrometer width) provide strong and stiff links between the ceramic layers (Fig. 3b and c). The brick-and-mortar materials mimic the structure of nacre at several length scales, in that they display larger ceramic contents, thin polymer layers, a characteristic interfacial roughness and a relatively large density of these thin inorganic bridges. However, they are still an order of magnitude coarser than the natural material.

3.2. Stress–strain curve behavior

Bending stress–strain curves for the Al_2O_3–PMMA hybrid materials replicate qualitatively those of nacre by showing >1% inelastic deformation prior to failure (Fig. 4a). The ultimate flexural strengths are summarized in Table 1. The strengths in the direction perpendicular to the ceramic layers are comparable to that of pure Al_2O_3, with average values of 116 and 210 MPa for the finest lamellae and brick-and-mortar structures, respectively (Table 1 and Fig. 4b and d). By comparison, the flexural strengths of pure Al_2O_3 and PMMA were found to be 325 ± 20 and 78 ± 5 MPa, respectively, while the fracture strength of hydrated nacre is 135 ± 4 MPa, consistent with previously reported data [28–32]. Decreasing the thickness of the ceramic layers had a slight effect on the flexural strengths (Fig. 4b). Furthermore, whereas increasing adhesion at the Al_2O_3–PMMA interface though chemical grafting resulted in a relatively small increase in the strength of lamellar structures, it had a very large effect (more than 80% increase) on the strength of the brick-and-mortar structures (Fig. 4).

3.3. Plane-strain fracture toughness, K_{IC}

The K_{IC} fracture toughness values for the hybrid materials, which represent a toughness for crack initiation, K_{IC}, were almost double of what could be expected from the simple “rule of mixtures” of the properties of the two constituents (Fig. 4c and d and Table 1). Refinement of the lamellae size slightly improved the initiation toughness of lamellar structures (Fig. 4c). As for the strength properties, grafting of the Al_2O_3–PMMA interface also resulted in a small increase of K_{IC} for the lamellar structures (Fig. 4c), but in a significant enhancement in toughness (almost 70%) for brick-and-mortar structures (Fig. 4d).

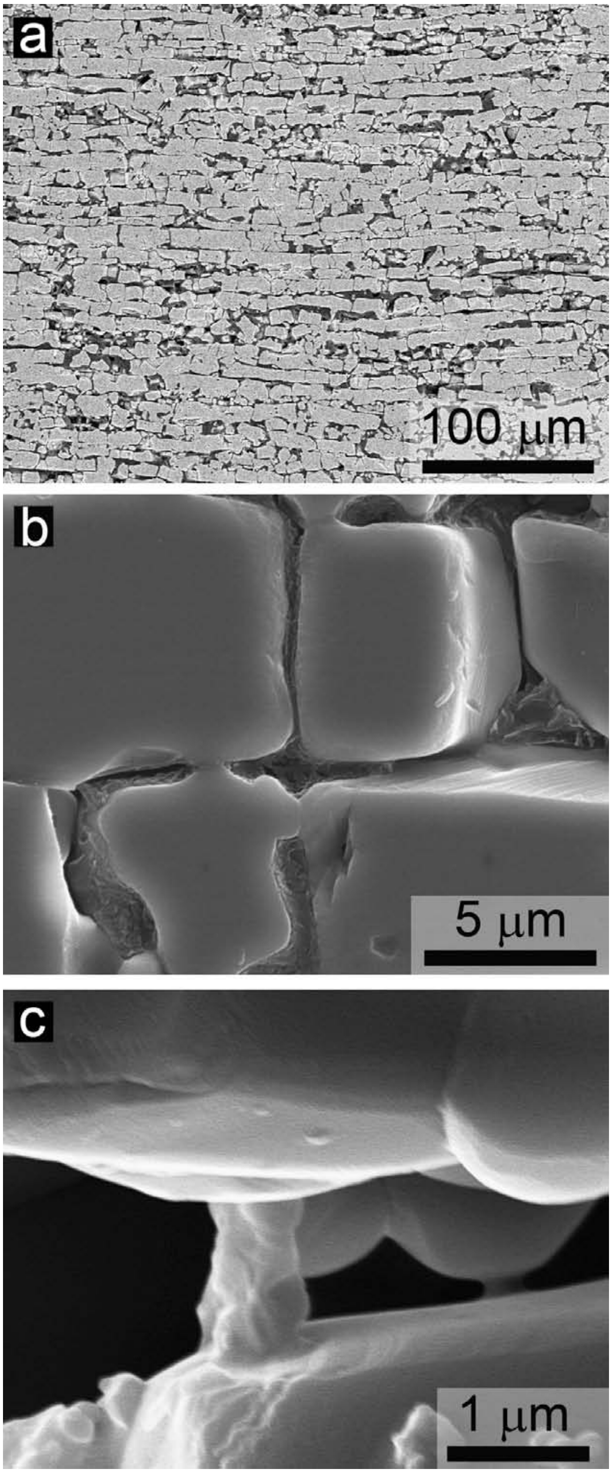

Fig. 3. (a) Brick-and-mortar architectures with large ceramic contents up to 80 vol.% are prepared through pressing of the lamellar materials and subsequent sintering. (b) These structures display large areas with submicrometer polymer films between alumina blocks. (c) Ceramic bridges between bricks are formed during the second sintering steps.

3.4. Resistance-curve behavior

The load-line displacement data (e.g. Fig. 5a) were analyzed to evaluate the $J_R(\Delta a)$ resistance curves. Typical results for the grafted brick-and-mortar structures are shown in Fig. 5b. According to active ASTM standards [21], the maximum J capacity for a specimen is given by the smaller of $J_{max} = b\sigma_y/20$ or $B\sigma_y/20$; similarly, the maximum crack extension capacity is given by: $\Delta a_{max} = 0.25b$. The J–R curve is therefore defined as the data in a region bounded by these J_{max} and Δa_{max} limits; for example, the maximum measurement capacity of the brick-and-mortar specimens were $J_{max} = 15\ \mathrm{kJ\ m^{-2}}$ (with $B = 1.5$ mm) and $\Delta a_{max} = 0.4$ mm (with $b = 1.6$ mm), as illustrated in Fig. 5b. The ASTM standards provide a somewhat arbitrary conservative limit. However, we can define a critical toughness, J_c, using a physical criterion as the maximum valid J-integral before the measurement become geometry dependent due to large-scale bridging (Fig. 5b). This criteria yields J-integral values that are slightly above the maximum crack extension, Δa_{max}, but have a clear physical meaning. Most importantly, the conditions for J-dominance were met in all the tests such that $b, B \geqslant 25\ (J_c/\sigma_y)$. This latter criterion ensures that the J-integral values represent valid fracture toughness values.

The R-curves can also be expressed with a K-based description (termed K_J), using the nominal mode I J–K equivalence $K_J = (J \cdot E')^{1/2}$, with $E' = E/(1 - \nu^2)$ in plane strain (ν is Poisson's ratio). These calculations require knowledge of the Young's modulus. The structure of the lamellar and brick-and-mortar hybrid composites is clearly directional; properties are orthotropic, with values of E lying between the upper and lower bound of the "rule of mixtures", as defined by the Reuss and Voigt models. Measurements using three-point bend tests showed that the elastic modulus values fell approximately at the mid-point between these upper and lower bounds. Using E values for PMMA of 3 GPa and for Al_2O_3 of 300 GPa, the elastic moduli for the lamellar and brick-and-mortar hybrid structures at 35 and ~80 vol.% ceramic content were calculated to be 57 and 115 GPa, respectively, in the direction perpendicular to the ceramic layers. These values were confirmed experimentally by contact ultrasonic measurements using a pulse–echo overlap technique with MHz shear and longitudinal piezoelectric transducers, and a pulser/receiver to measure the shear and longitudinal wave speeds at room temperature. Note that a relatively small error in the value of E has only a very limited impact on the computed K_J toughness; specifically, $a \pm 20\%$ error on E results in just $a \pm 1\%$ error in K_J.

R-curves are shown in Fig. 6 in terms of the equivalent stress intensity, K_J, as a function of crack extension, Δa, for the lamellar (Fig. 6a) and brick-and-mortar (Fig. 6b) hybrid composites. It is apparent that both natural (nacre) and synthetic composites exhibit marked rising R-curve behavior indicative of extensive extrinsic toughening. The degree of toughening in the hybrid composites actually surpasses that of nacre (the often cited "gold standard" in biomimetic design). The grafted Al_2O_3–PMMA lamellar and brick-and-mortar structures reach (steady-state) fracture toughnesses K_{Jc} of up to $15\ \mathrm{MPa\ m^{1/2}}$ ($J_c \sim 5\ \mathrm{kJ\ m^{-2}}$) and $30\ \mathrm{MPa\ m^{1/2}}$ ($J_c \sim 8\ \mathrm{kJ\ m^{-2}}$), respectively (Table 1).

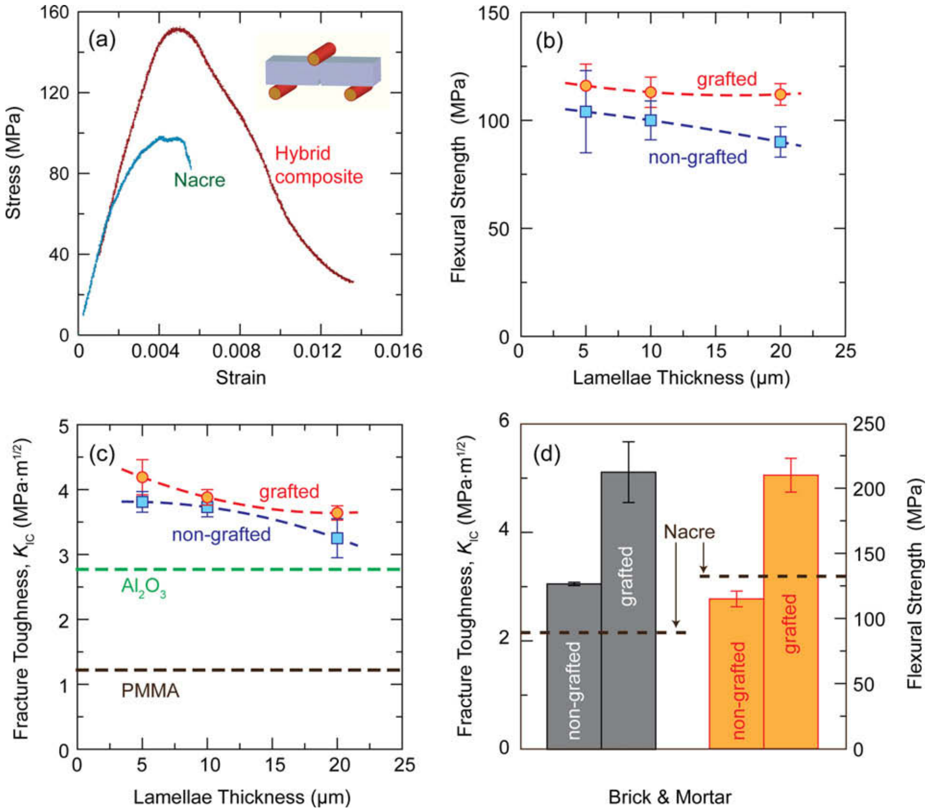

Fig. 4. (a) Bending stress–strain curves for the Al_2O_3–PMMA hybrid materials mimic those of nacre, and show >1% inelastic deformation prior to failure. The curves correspond to non-grafted lamellar hybrid composite and hydrated nacre (abalone shell). The role of the interfacial chemistry (grafting) in raising the interface energy is illustrated for both the lamellae and brick-and-mortar structures. Grafting increases both the (b) strength and (c) crack-initiation toughness, K_{IC}, of the lamellar composites. (d) This improvement is much more pronounced in the brick-and-mortar structure.

Table 1
Mechanical properties of the hybrid composites. The properties listed are crack-initiation fracture toughness (K_{IC}), flexural strength (σ_f) and crack-growth fracture toughness at instability (K_{Jc}).

Structure/ ceramic content	Interfacial chemistry	Lamellae/ brick thickness (μm)	K_{IC} (MPa m$^{1/2}$)	σ_f (MPa)	K_{Jc} (MPa m$^{1/2}$)
Lamellar 36 vol.%	Non-grafted	20	3.2 ± 0.3	90 ± 7	12 ± 2
		10	3.7 ± 0.1	100 ± 9	
		5	3.8 ± 0.2	104 ± 19	
	Grafted	20	3.6 ± 0.1	112 ± 5	16 ± 2
		10	3.9 ± 0.1	113 ± 7	
		5	4.2 ± 0.3	116 ± 10	
Brick-and-mortar 80 vol.%	Non-grafted	5	3.1 ± 0.1	115 ± 6	15 ± 2
	Grafted		5.1 ± 0.6	210 ± 13	32 ± 5

The latter is an outstandingly high toughness for a material consisting of 80% alumina with strength above 200 MPa; it is far in excess of the toughness of either constituent, and we believe that it is probably the toughest ceramic material reported to date. Indeed, the K_{Jc} toughness of the grafted brick-and-mortar hybrid materials is an order of magnitude higher than the standard hot-pressed homogeneous nanocomposites consisting of 500 nm Al_2O_3 particles dispersed in 55 vol.% PMMA. Similar to the fine-grained (1 μm) alumina, these homogeneous Al_2O_3–PMMA composites display minimal extrinsic toughening and consequently no rising *R*-curve behavior with very low fracture toughness below 2 MPa m$^{1/2}$.

As for the strength and crack-initiation toughness properties, grafting only offers a marginal increase in K_{Jc} for the lamellar materials (Fig. 6a), but a significant enhancement (a factor of 2 higher) for the brick-and-mortar structures (Fig. 6b). Refinement of the lamellae width did not affect the *R*-curve behavior of the lamellar composites and yielded similar K_{Jc} values (Fig. 6a).

3.5. Crack-growth observations

Stable crack growth during the *R*-curve measurements provides an opportunity to observe directly the toughening mechanisms and their relationship to the characteristic features of the microstructure. By performing these tests in situ in the scanning electron microscope, it is possible to measure the *R*-curve while simultaneously monitoring the evolution of damage mechanisms ahead of the crack tip and the extrinsic shielding mechanisms acting in the wake. Figs. 7 and 8 show typical examples of crack growth in the lamellar and brick-and-mortar architectures, respectively. Several mechanisms are clearly visible: (i) extensive inelastic deformation resulting in a wide (millimeter-scale)

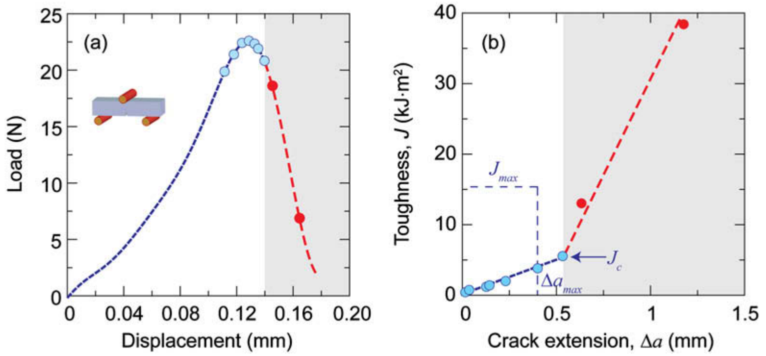

Fig. 5. (a) Typical load vs. load-line displacement curve, and (b) $J_R(\Delta a)$–R curve for stable crack extension in the grafted brick-and-mortar composite. The validity of the data points is defined by the measurement capacity of each specimen in accordance with ASTM standards [21]. The critical toughness, J_c, here was defined as the maximum J-integral before the test data becomes geometry-dependent due to large-scale bridging (i.e. crack-wake bridging zones are no longer small compared to the in-plane specimen dimensions).

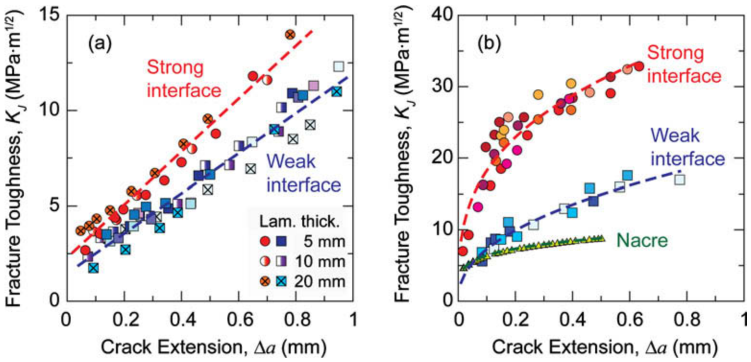

Fig. 6. Crack-resistance curves showing resistance to fracture in terms of the stress intensity, K_J, as a function of crack extension, Δa, for the (a) lamellar, and (b) brick-and-mortar hybrid Al_2O_3–PMMA composites. The fracture toughness, K_J, is back-calculated from the J measurements, shown in Fig. 4, using the J–K equivalence for mode I fracture (see text). R-curve data for natural nacre (abalone shell) are adapted from Ref. [6].

distribution of damage around the crack tip (Figs. 7a and 9)—this damage principally takes the form of micrometer-scale cracking of ceramic layers outside of the main crack path (Figs. 7a and 9); (ii) inelastic deformation within the polymer in the form of micrometer-scale tearing (Figs. 7 and 8); and (iii) elongated voids within the polymeric interlayers of lamellar materials, many of which result from the processing, but which appear to promote local plastic flow and grow during loading (Fig. 7a). These brittle and ductile damage processes appear to be quite distinct with little evidence of interaction.

The presence of such damage initiated ahead of (and distinct from) the main growing crack leads to the formation of uncracked-ligament bridging [33,34] in the wake of the crack tip. These elastic bridges, which are quite distinct from the pre-existing stiff ceramic bridges between layers and bricks, are formed in situ before the main growing crack links to the microcracks and voids; the bridges effectively span the crack and carry load that would otherwise be used to promote macroscopic crack advance.[1] In addition, the brick-and-mortar materials show clear evidence of polymer tearing and stretching over micrometer dimensions, and “pull out” via frictional sliding between ceramics bricks (Fig. 8).

Post-mortem examination of the fracture surfaces of the lamellar and brick-and-mortar composites after R-curve testing illustrates the effect of chemical grafting on the degree of delamination at the organic–inorganic interface during fracture (Fig. 10a and c). Better adhesion due to chemical grafting limits delamination and the resulting fracture surfaces are comparatively much flatter (Fig. 10b and d).

4. Discussion

Both lamellar and brick-and-mortar materials are strong and tough and display >1% inelastic strains when loaded in tension (Fig. 4a). The bending strengths are comparable to that of the ceramic, and the initiation toughnesses are well above that of the alumina or PMMA. The refinement in lamellar spacing slightly improved both the strength and K_{IC} fracture toughness (Fig. 4b and c). This implies that flaws in the material control the strength and subsequently the initiation toughness, with the thicker lamellae representing a larger sampling volume and a higher probability of finding a large flaw. However, what distinguishes the

---

[1] Instead of crack extension being solely associated with the main crack tip growing forward, crack advance also occurs by microcracks (or other damage) initiated ahead of the main crack tip linking back to the tip.

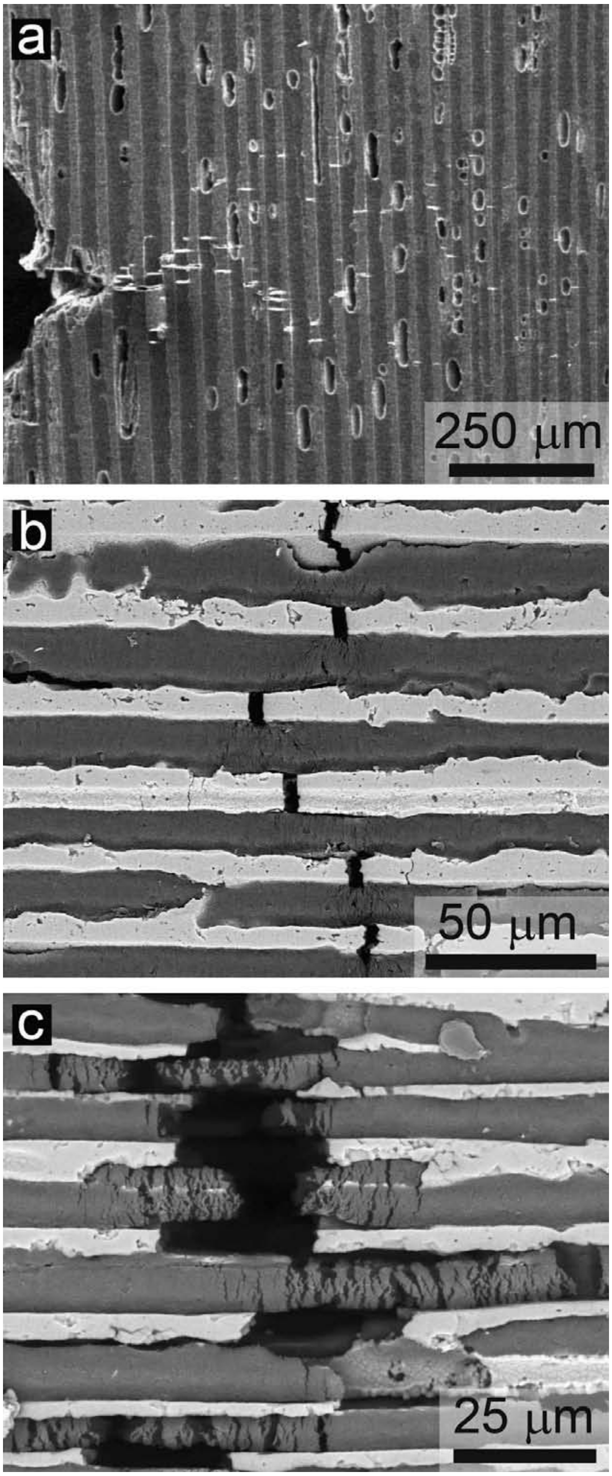

Fig. 7. Scanning electron micrographs taken during in situ *R*-curve measurements of the toughness of a lamellar Al_2O_3–PMMA structure. The image taken during stable crack propagation shows the toughening mechanisms acting at multiple length scales: (a) wide distribution of damage over millimeter dimensions in the form of contained microcracking within the ceramic and the voids in the polymer layers, (b) ductile uncracked-ligament bridging, and (c) inelastic deformation within the polymer in the form of micrometer-scale tearing.

freeze-cast materials is that, like natural composites, they clearly exhibit extensive subcritical crack growth during rising *R*-curve behavior indicative of significant extrinsic toughening. While single-value linear-elastic parameters based on crack initiation, such as K_{IC}, have traditionally been used to quantify toughness, they cannot capture, or even represent, the multiple length-scale toughening acting in these materials [9]. Evaluating their toughness requires nonlinear-elastic fracture mechanics to characterize the contributions from inelastic deformation, and more importantly, *R*-curve analysis to characterize the toughness associated with crack growth, both of which are afforded by the use of the *J*–*R* curve.

The in situ analysis of crack growth clearly shows how control of the structural architecture at several length scales permits the generation of multiple toughening mechanisms operating over a large range of dimensions; this creates extensive crack-tip shielding and unprecedented fracture resistance for a ceramic-based material. Observed toughening mechanisms include uncracked-ligament bridging in the crack wake (Figs. 7 and 9), grain bridging/pull-out, microcracking, crack deflection/delamination, void growth and the fracture of (pre-existing) ceramic bridges at the micrometer scale, and inelastic deformation of the polymer at submicrometer scales and higher; moreover, the extent of the damage is not localized but rather shows a wide distribution over millimeter dimensions. The elongated voids in the polymeric layer can act as very effective local crack arresters, in accord with the well-known Cook–Gordon mechanism [35] in laminates, and the energy dissipation to break the resulting crack bridges leads to ductile-phase toughening [36]. These mechanisms have clear parallels in natural structures such as cortical bone and tooth dentin [7,37], not to mention rocks as well as polymer and metal–matrix composites [33].

As in the lamellar materials, the brick-and-mortar microstructures exhibit extensive elastic bridging; however, unlike the lamellar materials there is little or no fracture of the ceramic bricks, rather there is some degree of “pull-out” between the bricks which in many respects replicates at microscopic dimensions the nanoscale phenomena observed in nacre (Fig. 8) [38]. This form of toughening is particularly potent and the prime source of the fracture resistance of most monolithic structural ceramics with engineered grain boundaries, i.e. coarse-grained Al_2O_3, Si_3N_4 and SiC [39–46]. Nevertheless, the contribution from bridging alone does not account for the unusually high toughness of the brick-and-mortar structure. There is a key distinction between the lamellar and brick-and-mortar materials that leads to critical differences in the nature and relative contribution of the different toughening mechanisms. In lamellar structures, the relatively thick polymer layer still plays a structural, load-bearing role. Conversely, the brick-and-mortar structure has a high ceramic content and the thin organic phase is not load bearing, akin to many hard mineralized natural composites; rather it acts as the “lubricant phase” and controls the sliding of the load-bearing ceramic blocks (Fig. 8). In this respect, the lubricant phase plays a role similar to dislocations in met-

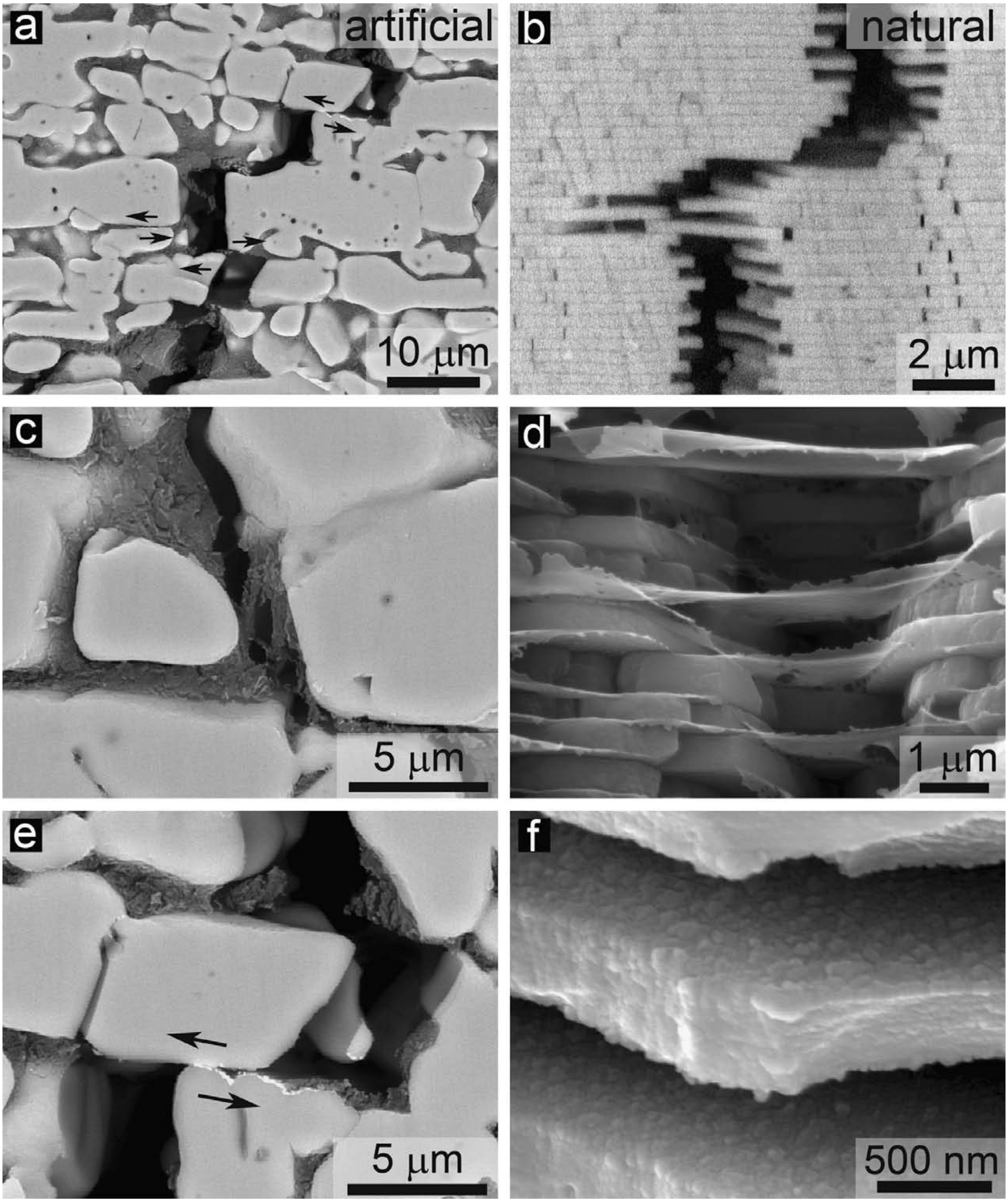

Fig. 8. Similarities between the toughening mechanisms acting in artificial (Al_2O_3–PMMA) and natural nacre. Scanning electron micrographs taken during an in situ *R*-curve measurement of (a, c and e) a grafted brick-and-mortar structure and (b, d and f) of hydrated nacre (abalone shell) show similar mechanisms although the nacre clearly has a finer structure. The image taken during stable crack propagation shows the toughening mechanisms acting at multiple length scales: (a) "pull out" mechanisms similarly to that observed in (b) nacre, (c) polymer tearing and stretching over micrometer dimensions as also observed in the (d) organic phase of nacre, and (e) frictional sliding resisted by the interface roughness of the ceramic bricks as observed in (f) nacre. Note that the thin bright lines between the sliding grains in (e) results from the deformation of the gold coating during sliding; indeed, all the mechanisms described above are rendered visible by electrical charging in the SEM resulting from the deformation of the gold coating during deformation.

als or microcracking in rocks in that it acts to relieve high stresses in the structure, thereby reducing the risk of fracture. As a result chemical grafting has a much larger effect on the brick-and-mortar structures; the stronger grafted interface enables the organic layer to act as a more effective viscoelastic glue, i.e. permitting yet limiting the extensive of

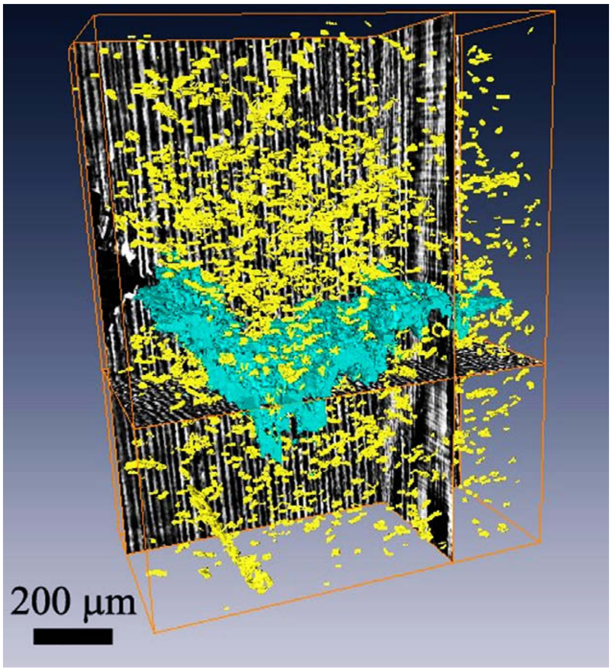

Fig. 9. Synchrotron X-ray tomography image of crack propagation from a sharpened notch (on the left-hand side) during an *R*-curve test of a lamellar Al_2O_3–PMMA composite, showing the wide distribution of damage (in yellow) spread over several millimeters surrounding the deflected crack path (in blue). Crack propagation is nominally from left to right. (For interpretation of color mentioned in this figure the reader is referred to the web version of the article.)

interfacial sliding, as in nacre (Fig. 8). In contrast, grafting has a very limited role in lamellar materials where the polymer has a structural function. The roughness of the ceramic interfaces and the presence of stiff (pre-existing) ceramic bridges between grains with micrometer and submicrometer dimensions (Figs. 2 and 3) also contribute to the controlled sliding ("sliding interference") between the rough ceramic layers (Fig. 8), thereby enhancing the toughness through extremely efficient energy dissipation. The result is a synthetic material which, like nacre, is far tougher that what could be expected from the simple mixture of its constituents (Fig. 11).

Two key design concepts emerge from the examination of these biomimetic, freeze-cast hybrid structures: the need of multiscale hierarchical architectures and the use of soft (non-load-bearing) phases that can act as a "lubricant". These concepts are quite different to those employed in other recent studies to develop improved structural composites, which of late have largely focused on the use of nanoscale reinforcements such as carbon nanotubes (with their near-ideal strength and extreme stiffness), platelets or nanofibers to increase toughness [47]. Although it has been claimed that materials reinforced at the nanoscale would have exceptional properties, results to date have been disappointing [48]. If the composite is to be used for a small-volume structure, clearly the reinforcements must also be small; moreover, small-volume reinforcements tend to be much stronger, as has been known since the early days of research on whiskers [49]. However, from the perspective of toughening, the use of the other larger length scales should not be ignored; nanoscale reinforcements alone are not the best direction to take [50,51]. The prime extrinsic toughening mechanisms, namely crack deflection and particularly crack bridging, are promoted by increasing, not decreasing, reinforcement dimensions [52], as is illustrated in the present work by the lack of toughening observed in the Al_2O_3–PMMA homogeneous nanocomposites (Fig. 11).

Large reinforcements in the form of fibers or particles have been successfully used to increase fracture resistance [57]. Crack bridging is again the most prominent toughening mechanism, particularly in ceramic–matrix composites. This mechanism is enhanced by utilizing fibers with weak fiber–matrix bonding; when the matrix fails, the fibers are left intact spanning the crack wake and can act as bridges to inhibit crack opening [52–55]. With continuous-fiber reinforced polymer composites, i.e. carbon-fiber-reinforced polymers, high volume fractions of graphite fibers with strong matrix–fiber interfaces are added for strength and stiffness. In all these structures, it is generally difficult to achieve both high strength and high toughness; the trade-off comes in part from the fact that both the matrix and the reinforcement play a load-bearing role and weakening the interfaces to promote crack path deflection also weakens the structure. With the current naturally inspired composites, freeze-cast lamellar materials exhibit layer thicknesses that can be almost an order of magnitude thinner than those of soft–hard composites prepared by conventional techniques [56–60]. As a result they can raise the degree of extrinsic toughening to values comparable, or even superior, to those of fiber-reinforced composites without any loss in strength. However, it is the brick-and-mortar Al_2O_3–PMMA structures, where the soft polymeric phase is no longer structural but serves as a stress-relieving lubricant, that provide the optimum combination of strength and toughness; these structures best illustrate the unique advantages and opportunities enabled by biomimetic design.

5. Summary and conclusions

Using the inspiration of natural materials, specifically nacre, we have developed a suite of ceramic-based hybrid materials with unprecedented combinations of strength and toughness, which when normalized with respect to the density is comparable to those of metallic aluminum alloys [16]. This has been achieved through careful manipulation of structural architecture to replicate many of the features underlying the unique properties of nacre, in particular its characteristic *R*-curve behavior which derives from a confluence of toughening mechanisms that emulate those of nacre over multiple length scales. Like in nacre, our best synthetic materials reflect the natural concept of a hard ceramic phase providing for material strength, separated by a softer "lubricant" phase to relieve high

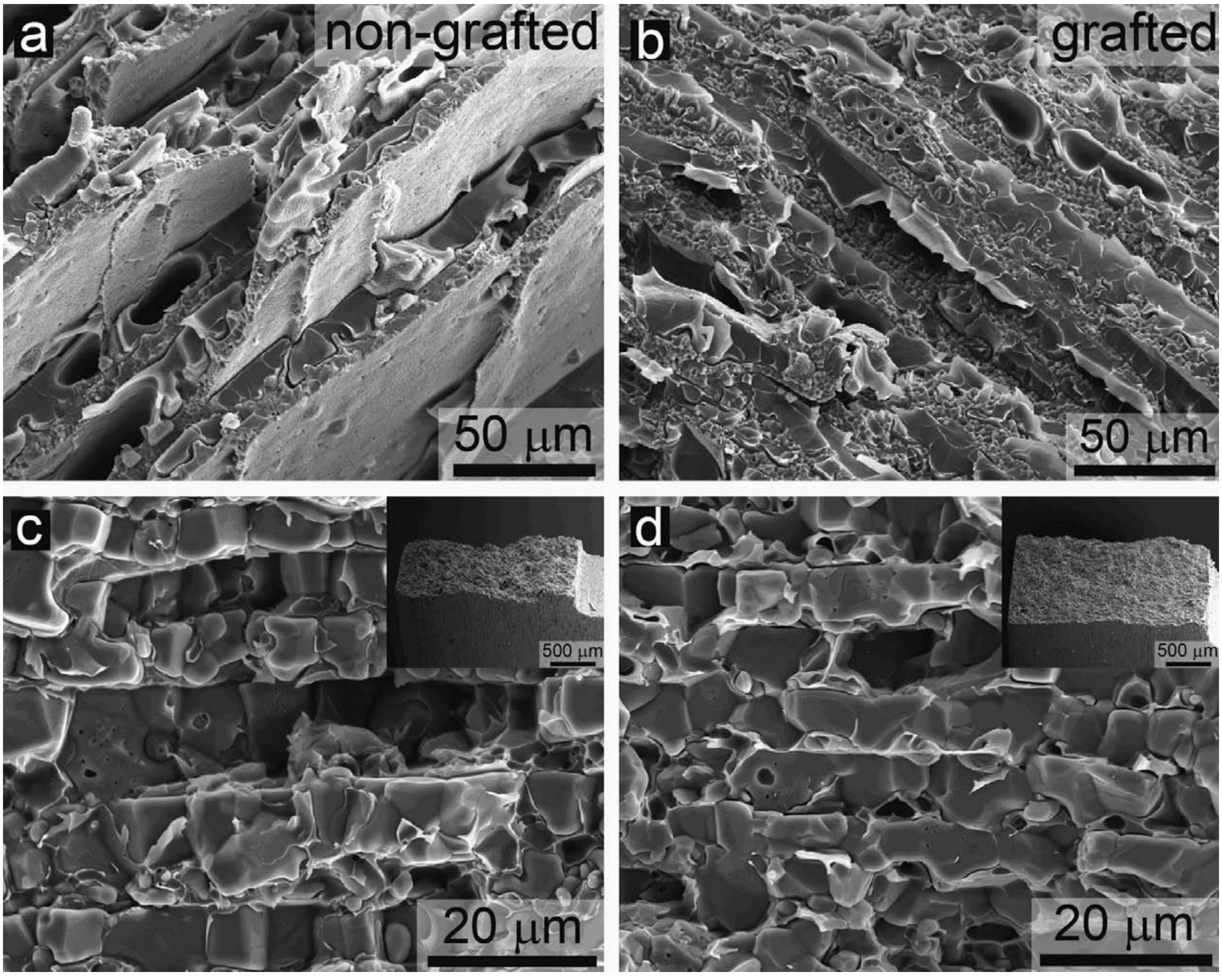

Fig. 10. Scanning electron micrographs of the fracture surfaces of (a and b) lamellar and (c and d) brick-and-mortar Al_2O_3–PMMA composites. (a and c) Non-grafted interfaces (which lead to weaker boundaries) show extensive interface delamination during fracture, while (b and d) chemical grafting results in better adhesion (stronger boundaries) and fracture surfaces that are comparatively much flatter.

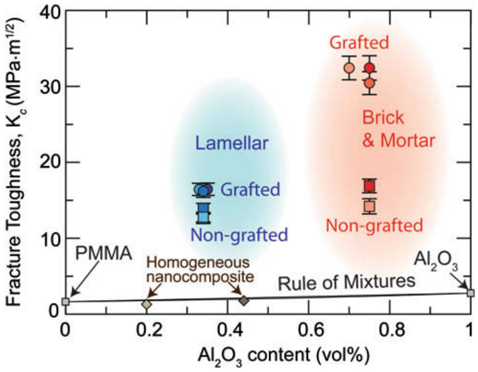

Fig. 11. *J*-based measurements of the fracture toughness for of the lamella and brick-and-mortar Al_2O_3–PMMA composites, showing their exceptional fracture toughness as compared to that of their constituent phases. The toughness of the pure components, along with that from the rule of mixtures, and K_{Jc} measurements for Al_2O_3–PMMA homogeneous nanocomposites, are also shown.

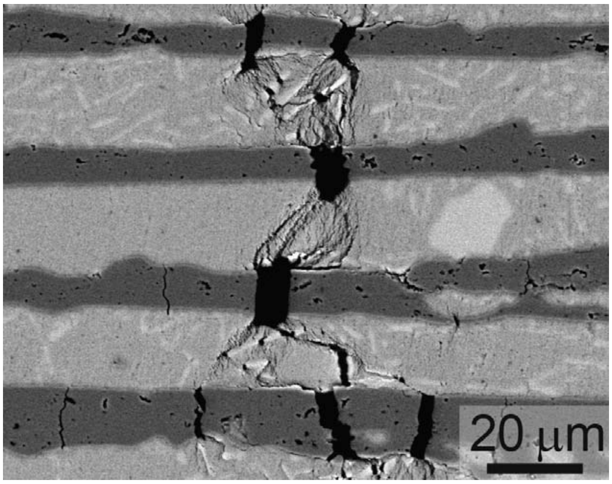

Fig. 12. Back-scattered electron micrograph of a ceramic–metal composite, here Al_2O_3/Al–Si, with a lamellar microstructure containing 36 vol.% of ceramic. The bright phase is Al–Si ($d \approx 20$ µm), and the dark phase is Al_2O_3 ($d \approx 10$ µm). Some of the observed toughening mechanisms, i.e. ductile uncracked-ligament bridging and tearing, are similar to those observed in the polymer–ceramic hybrid composites.

stresses in order to enhance toughness. The result is the highest toughness ceramic reported to date, with a strength of 200 MPa and a fracture toughness that is

$\sim$300 times (in J-terms) larger than the main constituent, Al_2O_3, and exceeds values of 30 MPa m$^{1/2}$ ($J_c \sim$ 8000 J m^{-2}).

Future work is being directed towards the formation of hybrid materials with much higher inorganic contents, the manipulation of the properties of the soft lubricating phase and extending this concept to other material combinations. In particular, we are attempting to process ceramic scaffolds infiltrated with higher melting point metals with the objective of developing strong and tough ceramic-based materials that can operate at elevated temperatures. Preliminary investigations on lamellar ceramic/metal materials, i.e. Al_2O_3/Al–Si (Fig. 12), show promising properties, specifically that their strength and toughness significantly exceeds the rule of mixtures of the properties of the two constituent phases.

Acknowledgments

This work was supported by the Director, Office of Science, Office of Basic Energy Sciences, Division of Materials Sciences and Engineering, of the US Department of Energy under Contract No. DE-AC02-05CH11231. We acknowledge the assistance of the X-ray microtomography beamline (8.3.2) at the Advanced Light Source (ALS) at Lawrence Berkeley National Laboratory. The authors also thank Prof. Daryl Chrzan and Mark Jhon for many helpful discussions, and Dr. Mary Laura Lind and Prof. William L. Johnson at the California Institute of Technology for the elasticity measurements.

References

[1] Mayer G. Science 2005;310:1144.
[2] Ortiz C, Boyce MC. Science 2008;319:1053.
[3] Fratzl P, Weinkamer R. Prog Mater Sci 2007;52:1263.
[4] Meyers MA, Chen PY, Lin AYM, Seki Y. Prog Mater Sci 2008;53:1.
[5] Aizenberg J, Weaver JC, Thanawala MS, Sundar VC, Morse DE, Fratzl P. Science 2005;309:275.
[6] Barthelat F, Espinosa HD. Exp Mech 2007;47:311.
[7] Nalla RK, Kruzic JJ, Kinney JH, Ritchie RO. Biomaterials 2005;26:217.
[8] Ritchie RO. Mater Sci Eng A 1988;103:15.
[9] Launey ME, Ritchie RO. Adv Mater 2009, in press. doi:10.1002/adma.200803322.
[10] Hartgerink JD, Beniash E, Stupp SI. Science 2001;294:1684.
[11] Aizenberg J. Adv Mater 2004;16:1295.
[12] Tang ZY, Kotov NA, Magonov S, Ozturk B. Nat Mater 2003;2:413.
[13] Sellinger A, Weiss PM, Nguyen A, Lu YF, Assink RA, Gong WL, et al. Nature 1998;394:256.
[14] Podsiadlo P, Kaushik AK, Arruda EM, Waas AM, Shim BS, Xu JD, et al. Science 2007;318:80.
[15] Deville S, Saiz E, Nalla RK, Tomsia AP. Science 2006;311:515.
[16] Munch E, Launey ME, Alsem DH, Saiz E, Tomsia AP, Ritchie RO. Science 2008;322:1516.
[17] Fukasawa T, Ando M, Ohji T, Kanzaki S. J Am Ceram Soc 2001;84:230.
[18] Munch E, Saiz E, Tomsia AP, Deville S. J Am Ceram Soc 2009, in press.
[19] Abboud M, Turner M, Duguet E, Fontanille M. J Mater Chem 1997;7:1527.
[20] Fakunle ES, Aguilar ZP, Shultz JL, Toland AD, Fritsch I. Langmuir 2006;22:10844.
[21] ASTM E1820-06. Annual book of ASTM standards, vol. 03.01: Metals—Mechanical testing; Elevated and low-temperature tests; Metallography. West Conshohocken, PA: ASTM International; 2006.
[22] ASTM D790-03. Annual book of ASTM standards, vol. 08.01: Plastics (I). West Conshohocken, PA: ASTM International; 2003.
[23] Kinney JH, Nichols MC. Annu Rev Mater Sci 1992;22:121.
[24] Vlassenbroeck J, Dierick M, Masschaele B, Cnudde V, Hoorebeke L, Jacobs P. Nucl Instrum Methods Phys Res Sect A 2007;580:442.
[25] Mercury CS. Avizo™ 3D visualization framework. Chelmsford, MA.
[26] Deville S, Saiz E, Tomsia AP. Acta Mater 2007;55:1965.
[27] Deville S. Adv Eng Mat 2008;10:155.
[28] Currey JD. Proc R Soc London Ser B 1977;196:443.
[29] Jackson AP, Vincent JFV, Turner RM. Proc R Soc Lond Ser B 1988;234:415.
[30] Sarikaya M. Microsc Res Tech 1994;27:360.
[31] Menig R, Meyers MH, Meyers MA, Vecchio KS. Acta Mater 2000;48:2383.
[32] Wang RZ, Suo Z, Evans AG, Yao N, Aksay IA. J Mater Res 2001;16:2485.
[33] Shang JK, Ritchie RO. Metall Trans A 1989;20:897.
[34] Koester KJ, Ager JW, Ritchie RO. Nat Mater 2008;7:672.
[35] Cook J, Evans CC, Gordon JE, Marsh DM. Proc R Soc Lond Ser A 1964;282:508.
[36] Sigl LS, Mataga PA, Dalgleish BJ, McMeeking RM, Evans AG. Acta Metall 1988;36:945.
[37] Nalla RK, Kinney JH, Ritchie RO. Biomaterials 2003;24:3955.
[38] Lin AYM, Chen PY, Meyers MA. Acta Biomater 2008;4:131.
[39] Becher PF, Sun EY, Plucknett KP, Alexander KB, Hsueh CH, Lin HT, et al. J Am Ceram Soc 1998;81:2821.
[40] Cao JJ, MoberlyChan WJ, DeJonghe LC, Gilbert CJ, Ritchie RO. J Am Ceram Soc 1996;79:461.
[41] Kruzic JJ, Cannon RM, Ritchie RO. J Am Ceram Soc 2004;87:93.
[42] Kruzic JJ, Cannon RM, Ager JW, Ritchie RO. Acta Mater 2005;53:2595.
[43] Lange FF. J Am Ceram Soc 1973;56:518.
[44] Mai YW, Lawn BR. J Am Ceram Soc 1987;70:289.
[45] Padture NP, Lawn BR. J Am Ceram Soc 1994;77:2518.
[46] Swanson PL, Fairbanks CJ, Lawn BR, Mai YW, Hockey BJ. J Am Ceram Soc 1987;70:279.
[47] Ajayan PM, Tour JM. Nature 2007;447:1066.
[48] Ritchie RO, Dzenis Y. Science 2008;320:448.
[49] Kelly A. Strong solids. Oxford: Clarendon Press; 1966.
[50] Cox B, Yang QD. Science 2006;314:1102.
[51] Marshall DB, Cox BN. Ann Rev Mater Res 2008;38:425.
[52] Evans AG. J Am Ceram Soc 1990;73:187.
[53] Ishikawa T, Kajii S, Matsunaga K, Hogami T, Kohtoku Y, Nagasawa T. Science 1998;282:1295.
[54] Naslain R, Dugne O, Guette A, Sevely J, Brosse CR, Rocher JP, et al. J Am Ceram Soc 1991;74:2482.
[55] Davis JB, Marshall DB, Morgan PED. J Eur Ceram Soc 2000;20:583.
[56] Clegg WJ, Kendall K, Alford NM, Button TW, Birchall JD. Nature 1990;347:455.
[57] Marshall DB, Ratto JJ, Lange FF. J Am Ceram Soc 1991;74:2979.
[58] Saunders RA, Lekakou C, Bader MG. Compos Sci Technol 1999;59:983.
[59] Hwu KL, Derby B. Acta Mater 1999;47:545.
[60] Mekky W, Nicholson PS. Compos Pt B—Eng 2007;38:35.